

# Spin orientation and magnetostriction of $\text{Tb}_{1-x}\text{Dy}_x\text{Fe}_2$ from first principles

Christopher E. Patrick

*Department of Materials, University of Oxford,  
Parks Road, Oxford OX1 3PH, UK\**

George A. Marchant and Julie B. Staunton

*Department of Physics, University of Warwick, Coventry CV4 7AL, UK*

(Dated: July 31, 2020)

## Abstract

The optimal amount of dysprosium in the highly magnetostrictive rare-earth compounds  $\text{Tb}_{1-x}\text{Dy}_x\text{Fe}_2$  for room temperature applications has long been known to be  $x=0.73$  (Terfenol-D). Here, we derive this value from first principles by calculating the easy magnetization direction and magnetostriction as a function of composition and temperature. We use crystal field coefficients obtained within density-functional theory to construct phenomenological anisotropy and magnetoelastic constants. The temperature dependence of these constants is obtained from disordered local moment calculations of the rare earth magnetic order parameter. Our calculations find the critical Dy concentration required to switch the magnetization direction at room temperature to be  $x_c=0.78$ , with magnetostrictions  $\lambda_{111}=2700$  and  $\lambda_{100}=-430$  ppm, close to the Terfenol-D values.

---

\* christopher.patrick@materials.ox.ac.uk

## I. INTRODUCTION

The cubic Laves phase compound Terfenol-D ( $\text{Tb}_{1-x}\text{Dy}_x\text{Fe}_2$ ,  $x = 0.73$ ) has unparalleled magnetostrictive properties at room temperature, developing strains of 1600 ppm when a small magnetic field is applied and rotated between the [100] and [111] crystal directions [1–3]. Originally developed for sonar [4], Terfenol-D has a range of potential applications, including vibrational energy harvesting [5, 6], non-destructive testing [7] and multiferroic devices [8]. The latter concept couples magnetostrictive and piezoelectric materials to control electric polarization (or magnetization) with a magnetic (or electric) field, essential for magnetic sensors or magnetoresistive memory [9].

While remarkable for its magnetostriction, Terfenol-D does suffer from two drawbacks: it is brittle [10] and, due to its reliance on the critical heavy rare earths (REs) Tb and Dy, it is expensive [11]. Intense research has been aimed at finding new materials with reduced or zero RE content and better mechanical properties, with the notable successes of Fe-Ga and Fe-Al (Galfenol and Alfenol) [12, 13]. Computational modelling, adopting a first-principles (parameter-free) methodology, provides a complementary approach to experimentally searching for new materials, as well as understanding existing ones [14–19]. However, despite Terfenol-D’s huge importance as a magnetostrictive material, first-principles modelling has not yet been able to answer a basic question, namely: why is the optimum dysprosium content  $x=0.73$ ?

Experimentally, the question can be answered by considering the spin orientation phase diagram [20], which maps out the preferred (easy) direction of magnetization of  $\text{Tb}_{1-x}\text{Dy}_x\text{Fe}_2$  as a function of  $x$  and temperature  $T$ . At  $T=300$  K, for  $x \leq 0.6$  the easy direction is along [111]; for  $x \geq 0.9$ , it is [100]. The critical concentration  $x_c=0.73$  lies within the soft boundary between these two regions of the phase diagram, and corresponds to a low magnetocrystalline anisotropy (MCA). The low MCA is essential for the aforementioned applications, since then only a small field is needed to trigger a magnetostrictive response. It is also important to note that this critical concentration  $x_c$  reduces with temperature [20].

A first-principles understanding of Terfenol-D therefore requires calculating the spin orientation diagram. These have been calculated in the past using crystal field (CF) theory [20–24], which, although giving physical insight, requires parameters e.g. from experiment or point charge models, which are difficult to fit. For instance, Ref. 22 demonstrates how three

different sets of CF parameters can reproduce the same experimental magnetostriction curve for DyFe<sub>2</sub>. First-principles calculations are free of these parameters, but are often limited to describing stoichiometric compounds at zero temperature.

Here, we combine non-empirical first-principles calculations with the CF approach in order to calculate the spin orientation diagram of Tb<sub>1-x</sub>Dy<sub>x</sub>Fe<sub>2</sub> and the critical concentration  $x_c(T)$ . Our approach takes the recently-introduced yttrium-analogue method of calculating CF coefficients within density-functional theory (DFT) [25]— which is numerically stable and avoids problems traditionally associated with describing highly-correlated 4*f* electrons in DFT— and extends it to compute the phenomenological model parameters associated with magnetostriction. CF theory is then used to calculate the magnetocrystalline and magnetoelastic energies associated with these localized RE-4*f* electrons. We further include the magnetostrictive contribution from itinerant electrons using the finite temperature DFT-based formulation of the disordered local moment picture. Our calculated spin orientation diagram reproduces experimental measurements of the [111] and [100] easy directions over the full range of temperatures and concentrations. We find the critical concentration  $x_c$  to be 0.78 at room temperature with magnetostrictions  $\lambda_{111}=2700$  and  $\lambda_{100}=-430$  ppm, close to the Terfenol-D values.

The rest of our manuscript is organized as follows. Section II describes the theory behind our calculation of the spin orientation diagram. In particular, we introduce the phenomenological expression for the total energy as a function of magnetization direction and strain, and discuss the magnetocrystalline and magnetoelastic constants which enter this expression. We review how the contribution to these constants from RE-4*f* electrons can be connected to crystal field coefficients, and describe how these coefficients are obtained within DFT. We also discuss the disordered local moment calculations used to obtain the itinerant electron contribution and the temperature dependence of the RE-4*f* magnetic moments. We then present our results in Sec. III, consisting of the calculated magnetocrystalline and magnetoelastic constants of TbFe<sub>2</sub> and DyFe<sub>2</sub>, and then the composition and temperature-dependent spin orientation diagram, which is the main result of this work. Finally in Sec. IV we outline future research directions.

## II. METHODOLOGY

### A. Spin orientation at zero temperature

Our calculations are based on the following phenomenological expression for the energy of the crystal,

$$E(\hat{\boldsymbol{e}}, \boldsymbol{\varepsilon}) = E_{\text{el}}(\boldsymbol{\varepsilon}) + E_{\text{RE}}(\hat{\boldsymbol{e}}, \boldsymbol{\varepsilon}) + E_{\text{itin}}(\hat{\boldsymbol{e}}, \boldsymbol{\varepsilon}) \quad (1)$$

which consists of a magnetization-independent elastic energy  $E_{\text{el}}$ , a contribution  $E_{\text{RE}}$  originating from the  $4f$  electrons localized on the RE atoms, and  $E_{\text{itin}}$ , which originates from itinerant (delocalized) electrons.  $\boldsymbol{\varepsilon}$  represents the strain, with components written either in Cartesian form ( $\varepsilon_{xx}, \varepsilon_{xy}$  etc.) or as linear combinations of these ( $\varepsilon^\alpha, \varepsilon^{\gamma i}, \varepsilon^{ei}$ ), where  $\alpha, \gamma$  and  $e$  describe homogeneous, tetragonal and shear strain modes, respectively [26].  $\hat{\boldsymbol{e}}$  is a unit vector describing the orientation of the magnetization, which can be alternatively expressed as  $\hat{\boldsymbol{e}} = (\cos \phi \sin \theta, \sin \phi \sin \theta, \cos \theta)$ . The equilibrium strain and magnetization state is taken to be that which minimizes  $E(\hat{\boldsymbol{e}}, \boldsymbol{\varepsilon})$ .

The magnetization of the entire crystal can be seen as the sum of individual contributions from local magnetic moments, where each local moment with some magnitude  $\mu$  is associated with a magnetic atom [27]. At zero temperature, the local moments form an ordered magnetic structure. Raising the temperature introduces thermal disorder amongst the local moments which generally weakens the overall magnetization, until complete disorder is reached at the Curie temperature [27]. In the zero temperature case,  $\hat{\boldsymbol{e}}$  describes equivalently the orientation of a particular local moment *or* the orientation of the overall magnetization [28]. However, this equivalence does not hold at finite temperature, where the magnetic properties of the crystal are determined as an average over the fluctuating local moments. We concentrate initially on the zero temperature case. The generalization to finite temperature is discussed in Sec. II F. We now discuss each term in equation 1:

#### 1. Elastic energy

The elastic energy is quadratic in strain and depends on the three elastic constants  $c_{11}$ ,  $c_{12}$  and  $c_{44}$  [26, 29]:

$$E_{\text{el}}(\boldsymbol{\varepsilon}) = \frac{c_{11}}{2}(\varepsilon_{xx}^2 + \varepsilon_{yy}^2 + \varepsilon_{zz}^2) + c_{12}(\varepsilon_{yy}\varepsilon_{zz} + \varepsilon_{zz}\varepsilon_{xx})$$

$$+\varepsilon_{xx}\varepsilon_{yy}) + \frac{c_{44}}{2}(\varepsilon_{xy}^2 + \varepsilon_{yz}^2 + \varepsilon_{zx}^2) \quad (2)$$

Ideally we should calculate these constants from first principles. However, even obtaining zero temperature elastic constants for the stoichiometric end compounds TbFe<sub>2</sub> and DyFe<sub>2</sub> in DFT is not straightforward due to the difficulty in treating the RE-4*f* electrons [30]. Furthermore, the elastic constants are, in principle, dependent on composition and temperature. For simplicity we instead use a single set of elastic constant values of 141, 65 and 49 GPa for  $c_{11}$ ,  $c_{12}$  and  $c_{44}$ , for all compositions and temperatures. These values were measured experimentally for Tb<sub>0.3</sub>Dy<sub>0.7</sub>Fe<sub>2</sub> [26]. We have tested the sensitivity of our results to this choice by calculating spin orientation diagrams using different sets of elastic constant values which were either obtained from DFT or measured experimentally, for different compositions [30, 31]. The comparison is provided as an Appendix , and shows the sensitivity to be very weak.

## 2. RE-4*f* electron energy

The energy associated with the RE-4*f* electrons  $E_{\text{RE}}(\hat{\boldsymbol{e}}, \boldsymbol{\varepsilon})$  can be further partitioned as

$$E_{\text{RE}}(\hat{\boldsymbol{e}}, \boldsymbol{\varepsilon}) = E_{\text{mca}}(\hat{\boldsymbol{e}}) + E_{\text{me}}(\hat{\boldsymbol{e}}, \boldsymbol{\varepsilon}) \quad (3)$$

where the MCA energy  $E_{\text{mca}}(\hat{\boldsymbol{e}})$  depends only on the orientation of the RE-4*f* magnetic moment, and the magnetoelastic energy  $E_{\text{me}}(\hat{\boldsymbol{e}}, \boldsymbol{\varepsilon})$  couples this orientation to the strain. The MCA energy can be written as

$$E_{\text{mca}}(\hat{\boldsymbol{e}}) = \sum_{l=4,6} \mathcal{K}^{\alpha,l} S^{\alpha,l}(\hat{\boldsymbol{e}}) \quad (4)$$

where  $\mathcal{K}^{\alpha,l}$  are the anisotropy constants and  $S^{X,l}$  are the symmetry basis functions, which are listed in Ref. 26 ( $X = \alpha, \gamma, \epsilon$ ).  $\mathcal{K}^{\alpha,l}$  are related to the more conventional anisotropy constants  $K_1$  and  $K_2$  as  $K_1 = -2(\mathcal{K}^{\alpha,4} + \frac{1}{22}\mathcal{K}^{\alpha,6})$  and  $K_2 = \mathcal{K}^{\alpha,6}$ .

The magnetoelastic energy  $E_{\text{me}}(\hat{\boldsymbol{e}}, \boldsymbol{\varepsilon})$  is obtained as the direct product of strain and magnetization basis functions belonging to the same representation [26]:

$$\begin{aligned} E_{\text{me}}(\hat{\boldsymbol{e}}, \boldsymbol{\varepsilon}) &= \varepsilon^\alpha \sum_{l=4,6} \mathcal{B}^{\alpha,l} S^{\alpha,l}(\hat{\boldsymbol{e}}) \\ &+ \sum_{i=1,2} \varepsilon^{\gamma i} \sum_{l=2,4,6} \mathcal{B}^{\gamma,l} S_i^{\gamma,l}(\hat{\boldsymbol{e}}) \\ &+ \sum_{i=1,2,3} \varepsilon^{\epsilon i} \sum_{l=2,4,6,6'} \mathcal{B}^{\epsilon,l} S_i^{\epsilon,l}(\hat{\boldsymbol{e}}) \end{aligned} \quad (5)$$

The coefficients  $\mathcal{B}^{X,l}$  are the magnetoelastic constants. Note how the lower symmetry of the tetragonal or shear-strained structures ( $\gamma$  or  $\epsilon$ ) generates new terms with an  $l=2$  dependence on magnetization direction.

Evaluating  $E_{\text{RE}}(\hat{\boldsymbol{e}}, \boldsymbol{\varepsilon})$  therefore requires knowing the anisotropy and magnetoelastic constants  $\mathcal{K}^{\alpha,l}$  and  $\mathcal{B}^{X,l}$ . We discuss the calculation of these constants within the framework of the single-ion model and crystal field theory in Secs. II B, II C and II D.

### 3. Itinerant electron energy

The remaining term  $E_{\text{itin}}(\hat{\boldsymbol{e}}, \boldsymbol{\varepsilon})$  accounts for the MCA and magnetoelastic contributions to the energy not already included in the RE-4*f* term, i.e. those coming from itinerant electrons. These itinerant electrons are mainly Fe-3*d* in character, with a lesser contribution from the RE-5*d* electrons [14]. The relative importance of  $E_{\text{RE}}$  and  $E_{\text{itin}}$  to the magnetostriction can be assessed by comparing TbFe<sub>2</sub> or DyFe<sub>2</sub> to their isostructural counterpart GdFe<sub>2</sub>. These three compounds have the same itinerant electronic structure, and therefore should have comparable  $E_{\text{itin}}$ . However,  $E_{\text{RE}}$  is zero in GdFe<sub>2</sub> due to the filled Gd-4*f* spin subshell having zero orbital moment [32]. Comparing the experimentally-measured magnetostrictions of the different compounds, we find TbFe<sub>2</sub> has a magnetostriction which is 50 times larger than GdFe<sub>2</sub> [26], showing that  $E_{\text{RE}}$  is the dominant contribution to equation 1. Nevertheless, for completeness we still include  $E_{\text{itin}}$  in our analysis.

In principle,  $E_{\text{itin}}(\hat{\boldsymbol{e}}, \boldsymbol{\varepsilon})$  can be split into MCA and magnetoelastic contributions as in equation 3, with a different set of constants. In practice (Sec. III A), we find the MCA contribution to be negligible, and also that it is sufficient only to consider the  $l = 2$  term in the magnetoelastic expansion. We therefore have

$$E_{\text{itin}}(\hat{\boldsymbol{e}}, \boldsymbol{\varepsilon}) = \mathcal{B}_{\text{itin}}^{\gamma,2} \sum_{i=1,2} \varepsilon^{\gamma i} S_i^{\gamma,2}(\hat{\boldsymbol{e}}) + \mathcal{B}_{\text{itin}}^{\epsilon,2} \sum_{i=1,2,3} \varepsilon^{\epsilon i} S_i^{\epsilon,2}(\hat{\boldsymbol{e}}) \quad (6)$$

Due to their itinerant electron origin, the constants  $\mathcal{B}_{\text{itin}}^{\gamma,2}$  and  $\mathcal{B}_{\text{itin}}^{\epsilon,2}$  cannot be obtained from crystal field theory. They are however amenable to treatment in the DFT-based disordered local moment picture [27, 33]. We describe these calculations in Sec. II E.

## B. Single-ion treatment of RE-4*f* contribution and modelling of alloys

We calculate the RE-4*f* energy  $E_{\text{RE}}(\hat{e}, \boldsymbol{\varepsilon})$  within the single-ion model [34], which has been used to great effect to understand the behavior of RE-transition metal compounds for many years [32]. In this model, the magnetic moment associated with the 4*f* electrons localized on a particular RE ion behaves independently of its neighbours, which is a reasonable approximation [22] given the highly-localized nature of these electrons and the relatively weak RE-RE magnetic interactions measured in neutron scattering experiments [35]. The 4*f* electrons localized at different RE sites experience the same potential, which is an atomic-like central potential plus a contribution from the surrounding crystal field. The RE-4*f* electrons also all experience an exchange field originating from the itinerant electrons and possibly an external magnetic field, which both drive magnetic order [32].

The crystal field is supposed to derive from the valence electronic structure, and therefore is insensitive to (a) the orientations of surrounding RE-4*f* localized moments, and (b) the chemical species (Tb or Dy) of surrounding RE ions (since these species have the same  $6s^25d$  valence electronic structure). This latter aspect allows a simple treatment of Tb-Dy alloying within the single-ion model, since each RE ion is independent: for a given composition  $\text{Tb}_{1-x}\text{Dy}_x\text{Fe}_2$ , the RE-4*f* energy per ion is a superposition of the Tb and Dy contributions,

$$E_{\text{RE}}(\hat{e}, \boldsymbol{\varepsilon}) = (1 - x)E_{\text{Tb}}(\hat{e}, \boldsymbol{\varepsilon}) + xE_{\text{Dy}}(\hat{e}, \boldsymbol{\varepsilon}), \quad (7)$$

where now  $E_{\text{Tb}}$  and  $E_{\text{Dy}}$  can be seen as the RE-4*f* energy contributions calculated for the end compounds  $\text{TbFe}_2$  and  $\text{DyFe}_2$ , respectively. These end compounds each have their own set of two anisotropy and nine magnetoelastic constants, so to evaluate  $E_{\text{RE}}$  for an arbitrary  $x$  we require 22 constants in total.

## C. RE anisotropy and magnetoelastic constants from crystal field theory

In the single-ion central potential, the RE-4*f* electrons form atomic-like eigenstates  $|L, S, J, M_J\rangle$ , where  $L$  and  $S$  are determined by Hund's rules,  $J = L + S$  for Tb and Dy, and  $M_J = J, J - 1, \dots, -J$  [36]. Now, we should construct a Hamiltonian for the RE-4*f* electrons including the crystal, exchange and external fields, and diagonalize it within the manifold of states with different  $M_J$  [37]. Without the crystal and external fields, the ground state will be  $|L, S, J, -J\rangle$ , with the quantization axis (magnetic moment direction) aligned with

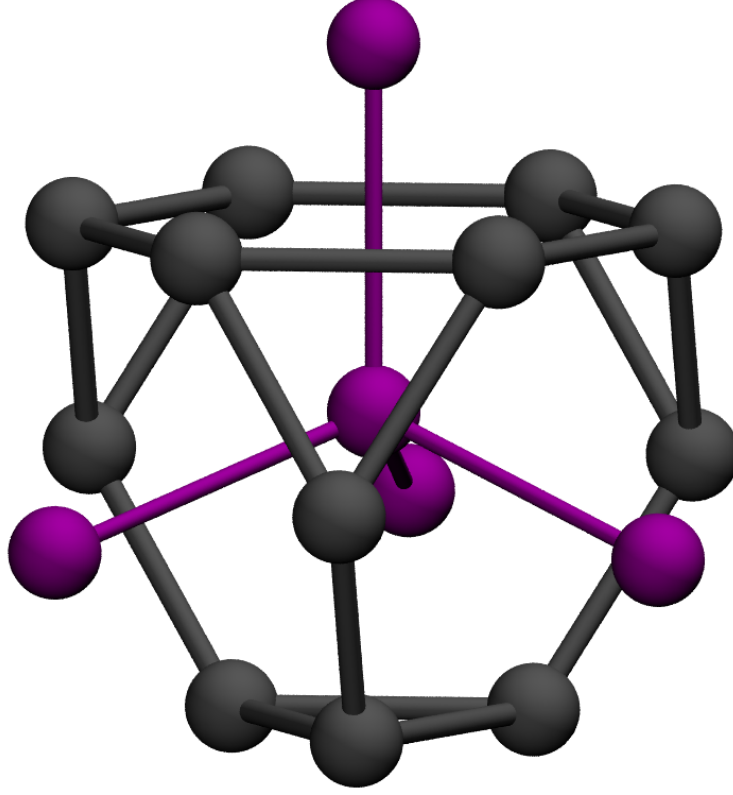


FIG. 1. The local  $T_d$  environment of the RE atom in the cubic Laves phase, showing nearest neighbor (Fe, grey) and next-nearest neighbor (RE, purple) atoms. The RE-RE bonds are oriented along the  $\langle 111 \rangle$  directions.

the exchange field. Taking this axis as  $\hat{z}$ , the RE-4*f* electron density  $\rho_{4f}^{(\hat{z})}(\mathbf{r})$  associated with  $|L, S, J, -J\rangle$  is given by [38]:

$$\rho_{4f}^{(\hat{z})}(\mathbf{r}) = n_{4f}^0(r) \sum_{l=2,4,6} \mathcal{A}_l \left( \frac{2l+1}{4\pi} \right)^{\frac{1}{2}} Y_{l0}(\hat{\mathbf{r}}) \quad (8)$$

Here,  $n_{4f}^0(r)$  is the radial density calculated for the unperturbed central potential [32], and  $Y_{lm}(\hat{\mathbf{r}})$  are complex spherical harmonics.  $\mathcal{A}_l$  are RE-dependent numerical factors formed from  $J$  and Stevens coefficients, which for  $\text{Tb}^{3+}$  are  $\mathcal{A}_2 = -(1/3)$ ,  $\mathcal{A}_4 = (1/11)$  and  $\mathcal{A}_6 = -(5/429)$ , and for  $\text{Dy}^{3+}$  are  $\mathcal{A}_2 = -(1/3)$ ,  $\mathcal{A}_4 = -(4/33)$ , and  $\mathcal{A}_6 = (25/429)$  [38, 39]. The RE-4*f* charge density  $\rho_{4f}^{(\hat{\mathbf{e}})}(\mathbf{r})$  corresponding to a general magnetic moment direction  $\hat{\mathbf{e}}$  is obtained from equation 8 by making the substitution  $Y_{l0}(\hat{\mathbf{r}}) \rightarrow \sum_m e^{-im\phi} d_{m0}^{(l)}(\theta) Y_{lm}(\hat{\mathbf{r}})$ , where the functions  $d_{m0}^{(l)}(\theta)$  are equal to  $[(l-m)!/(l+m)!]^{\frac{1}{2}} P_l^m(\cos\theta)$  and  $P_l^m(x)$  are the associated Legendre polynomials [40].



The crystal field (CF) characterizes the nonspherical components of the potential at the RE site,  $V(\mathbf{r}) = \sum_{lm} V_{lm}(r)Y_{lm}(\hat{\mathbf{r}})$ . If the exchange field is sufficiently strong compared to the CF, the latter will not mix states of different  $M_J$ . Then, the energy shift due to the CF is obtained from first order perturbation theory as

$$E_{4f}(\hat{\mathbf{e}}) = \sum_{l=2,4,6} \mathcal{A}_l \sum_m (-1)^m B_{l-m} e^{-im\phi} d_{m0}^{(l)}(\theta) \quad (9)$$

where the CF coefficients [25] have been introduced as:

$$B_{lm} = \left( \frac{2l+1}{4\pi} \right)^{\frac{1}{2}} \int r^2 n_{4f}^0(r) V_{lm}(r) dr. \quad (10)$$

For REFe<sub>2</sub> in the cubic Laves phase (Fig. 1), the RE atoms sit at sites with  $T_d$  symmetry, so the only nonzero CF coefficients which appear in equation 9 are  $B_{40}$ ,  $B_{4\pm 4}$ ,  $B_{60}$  and  $B_{6\pm 4}$ ; only  $B_{40}$  and  $B_{60}$  are independent [41].

Here we will assume that the exchange field is strong enough that  $E_{4f}(\hat{\mathbf{e}})$  is given by equation 9, and also that the exchange field and magnetization are isotropic. Then,  $E_{4f}$  is the only contribution to the energy which depends on the magnetization angle. At zero strain we can equate  $E_{4f}$  and  $E_{\text{mca}}$  (equations 4 and 9) to obtain

$$\mathcal{K}^{\alpha,4} = \frac{5}{2} \mathcal{A}_4 B_{40}; \quad \mathcal{K}^{\alpha,6} = \frac{231}{2} \mathcal{A}_6 B_{60}. \quad (11)$$

Next, to obtain the magnetoelastic constants  $\mathcal{B}^{X,l}$  we consider the modifications to the CF coefficients when three different strain modes are applied:  $\varepsilon_{xx} = \varepsilon_{yy} = \varepsilon_{zz} = \varepsilon_I$  (isotropic),  $\varepsilon_{zz} = -2\varepsilon_{xx} = -2\varepsilon_{yy} = \varepsilon_T$  (tetragonal) and  $\varepsilon_{xy} = \varepsilon_{yz} = \varepsilon_{zx} = \varepsilon_S$  (shear). For the shear deformation it is convenient to work in a rotated co-ordinate system where the  $z$  axis coincides with the [111] direction. Then, aside from altering the CF coefficients which are already nonzero in the unstrained  $T_d$  environment, the tetragonal and shear strains affect  $E_{4f}(\hat{\mathbf{e}})$  in equation 9 by generating a nonzero  $B_{20}$  coefficient.

Denoting the strain-induced shifts in CF coefficients as  $\Delta B_{lm}$ , our calculations (Sec. III A) find that these shifts can be described well by the linear relation  $\Delta B_{lm} = \frac{dB_{lm}}{d\varepsilon_X} \varepsilon_X$ . Inserting these relations into equation 9 and comparing to equation 5 gives each magnetoelastic constant in terms of the strain derivative of a CF coefficient, for instance,

$$\mathcal{B}^{\gamma,2} = \frac{2}{3} \mathcal{A}_2 \frac{dB_{20}}{d\varepsilon_T}; \quad \mathcal{B}^{\epsilon,2} = \mathcal{A}_2 \frac{dB_{20}}{d\varepsilon_S}. \quad (12)$$

#### D. DFT calculation of CF coefficients

Equations 11 and 12 show how the anisotropy and magnetoelastic constants can be obtained from the CF coefficients  $B_{lm}$  and their strain derivatives  $dB_{lm}/d\varepsilon_X$ . These are the quantities which we calculate from first principles within the yttrium-analogue method [25]. In this approach, the potential  $V(\mathbf{r})$  which determines the CF coefficients is calculated within DFT for the “Y-analogue” of  $\text{TbFe}_2$  or  $\text{DyFe}_2$ , which is  $\text{YFe}_2$ . Specifically, the components  $V_{lm}(r)$  in equation 10 are found from the angular decomposition of the self-consistent Kohn-Sham potential calculated for the desired  $\text{REFe}_2$  structure, where the RE is replaced with Y.

We have previously used the Y-analogue method to calculate CF coefficients for various RE/transition-metal compounds [25], demonstrating its applicability to describe temperature and pressure-induced spin-reorientation transitions in the  $\text{RECo}_5$  compounds [37, 42, 43]. Substituting Tb or Dy with Y to calculate the crystal field is consistent with the assumptions of the single-ion model [34], namely that the CF depends on the valence electronic structure and not on the RE-4*f* electrons themselves. Since the RE ions are in the 3+ state and therefore are isovalent (two *s* and a single *d* electron), we expect the CF of  $\text{YFe}_2$  to be a good approximation for  $\text{TbFe}_2$  or  $\text{DyFe}_2$ . Indeed, using the Y-analogue ensures that there is no double-counting of the RE-4*f* electrons in equation 10. Any DFT implementation can be used to calculate the CF coefficients, providing the valence charge density is described accurately.

Equation 10 also contains the RE-4*f* electron density calculated for the unperturbed central potential  $n_{4f}^0(r)$ . Previously we calculated  $n_{4f}^0(r)$  within self-interaction-corrected DFT [44, 45] for a number of compounds and found that, for a given RE element, it was highly insensitive to the crystalline environment [25]. Therefore when calculating CF coefficients we use the same previously calculated RE-dependent functions ( $n_{4f,\text{Tb}}^0(r)$  or  $n_{4f,\text{Dy}}^0(r)$  [46]) for all strain states.

#### E. Itinerant electron contribution

The itinerant electrons are (by definition) delocalized, and are responsible for generating the crystal field rather than simply being influenced by it. Accordingly, the CF picture is

not appropriate to describe their contribution to the magnetostriction. However, itinerant electron magnetism is amenable to a fully first-principles treatment within DFT [27]. In Sec. II A 3 we used  $\text{GdFe}_2$  as a comparison system to understand the importance of  $E_{\text{itin}}(\hat{\mathbf{e}}, \boldsymbol{\varepsilon})$  to the magnetostriction, since it has the same valence electronic structure but zero CF contribution from the filled Gd-4*f* spin subshell. Building on this idea, we take  $E_{\text{itin}}(\hat{\mathbf{e}}, \boldsymbol{\varepsilon})$  to be the same for  $\text{Tb}_{1-x}\text{Dy}_x\text{Fe}_2$  and  $\text{GdFe}_2$ , and calculate the latter directly. Similarly to using the Y-analogue, this approach avoids any double-counting of the CF contribution. However, using Gd rather than Y to calculate  $E_{\text{itin}}$  has the advantage of capturing any additional on-site polarization of the valence electrons by the large spin moments possessed by Gd, Tb and Dy [47, 48].

We calculate  $E_{\text{itin}}(\hat{\mathbf{e}}, \boldsymbol{\varepsilon})$  for  $\text{GdFe}_2$  using the same method demonstrated recently for bcc Fe and Fe-Ga alloys [33]. This approach is a Green's function, multiple-scattering theory-based formulation of the disordered local moment picture within DFT (DFT-DLM [27]) which as discussed in Sec. II F allows the treatment of finite temperature magnetic disorder. The filled Gd-4*f* spin subshell is treated efficiently using the local self-interaction correction (LSIC) [44]. Quantities related to the magnetic anisotropy are obtained by solving the relativistic single-site scattering problem and applying the torque method [49]. As described in Ref. [33], calculating the derivative of the total energy with respect to magnetization angle for different strain states allows the anisotropy and magnetoelastic constants to be obtained.

## F. Generalization to finite temperature

The methodology described above is sufficient to evaluate equation 1 assuming that all the individual magnetic moments are ordered, corresponding to zero temperature. At finite temperature  $T$ , equation 1 takes a slightly different form:

$$E(\hat{\mathbf{n}}, \boldsymbol{\varepsilon}, T) = E_{\text{el}}(\boldsymbol{\varepsilon}) + E_{\text{RE}}(\hat{\mathbf{n}}, \boldsymbol{\varepsilon}, T) + E_{\text{itin}}(\hat{\mathbf{n}}, \boldsymbol{\varepsilon}, T) \quad (13)$$

The new quantity introduced is the unit vector  $\hat{\mathbf{n}}$  which describes the orientation of the magnetization of the entire crystal, and therefore represents an average over the individual magnetic moments. The degree of magnetic order is quantified through the temperature-dependent order parameters  $m_{\text{Tb}}$ ,  $m_{\text{Dy}}$  and  $m_{\text{itin}}$  which take values between 1 (zero temperature, fully ordered) and 0 (above the Curie temperature, fully disordered). The relationship

between the orientation of the individual moments and their average is given by, for instance,  $\langle \hat{\mathbf{e}}_{\text{Tb}} \rangle_T = m_{\text{Tb}}(T) \hat{\mathbf{n}}$  where  $\langle \rangle_T$  denotes the statistical mechanical thermal average taken (in this example) over the individual moments of all Tb ions. More generally, the finite and zero temperature energies in equations 1 and 13 are related simply as  $E(\hat{\mathbf{n}}, \boldsymbol{\varepsilon}, T) = \langle E(\hat{\mathbf{e}}, \boldsymbol{\varepsilon}) \rangle_T$ .

Evaluating the thermal average  $\langle \rangle_T$  requires a model for the statistical mechanics of the magnetic moments. The DFT-DLM framework employs a Heisenberg-like Hamiltonian for this purpose [27]. The probability that a moment is aligned along a direction  $\hat{\mathbf{e}}$  at  $T$  is given by  $P_{\hat{\mathbf{n}}}(\hat{\mathbf{e}}) \propto \exp[\beta h \hat{\mathbf{n}} \cdot \hat{\mathbf{e}}]$ , where  $1/\beta = k_B T$ . The Weiss field felt by each local moment  $h(T)$  is determined self-consistently from DFT-DLM calculations at a given temperature using the iterative scheme described in Ref. [50]. The self-consistency condition ensures (a) that the free energy is minimized, and (b) that the model approximates the true statistical mechanics of the moments as closely as possible [27]. Each crystallographically inequivalent magnetic atom (Tb, Dy and Fe) experiences its own Weiss field, and within the model the order parameter and Weiss fields are linked according to (again taking Tb as an example):

$$m_{\text{Tb}}(T) = \coth(\beta h_{\text{Tb}}(T)) - \frac{1}{\beta h_{\text{Tb}}(T)} \quad (14)$$

### 1. Thermally-averaged rare earth contribution

Recalling that in the crystal field picture the CF is independent of the RE moment orientations, and that the anisotropy and magnetoelastic constants are determined by the CF coefficients, the thermal average of the RE contribution is determined solely by the average of the symmetry basis functions, e.g.

$$E_{\text{mca}}(\hat{\mathbf{n}}, T) = \sum_{l=4,6} \mathcal{K}^{\alpha,l} \langle S^{\alpha,l}(\hat{\mathbf{e}}) \rangle_T. \quad (15)$$

Due to the local nature of the probability function  $P_{\hat{\mathbf{n}}}(\hat{\mathbf{e}})$ , the general arguments of Callen and Callen [34] can be used to show

$$\langle S^{X,l}(\hat{\mathbf{e}}) \rangle_T = f_l(m) S^{X,l}(\hat{\mathbf{n}}) \quad (16)$$

where the functions  $f_l(m)$  depend on  $m$  as  $m^{\frac{l(l+1)}{2}}$  and  $m^l$  at low and high temperature respectively [34]. Then, the explicit expression for the RE contribution at finite temperature is

$$E_{\text{RE}}(\hat{\mathbf{n}}, \boldsymbol{\varepsilon}, T) = \sum_{l=4,6} \mathcal{K}_{\text{RE}}^{\alpha,l}(T) S^{\alpha,l}(\hat{\mathbf{n}})$$

$$\begin{aligned}
& + \varepsilon^\alpha \sum_{l=4,6} \mathcal{B}_{\text{RE}}^{\alpha,l}(T) S^{\alpha,l}(\hat{\mathbf{n}}) \\
& + \sum_{i=1,2} \varepsilon^{\gamma i} \sum_{l=2,4,6} \mathcal{B}_{\text{RE}}^{\gamma,l}(T) S_i^{\gamma,l}(\hat{\mathbf{n}}) \\
& + \sum_{i=1,2,3} \varepsilon^{\epsilon i} \sum_{l=2,4,6,6'} \mathcal{B}_{\text{RE}}^{\epsilon,l}(T) S_i^{\epsilon,l}(\hat{\mathbf{n}})
\end{aligned} \tag{17}$$

where the finite and zero-temperature constants are simply related by  $f_l$ ,

$$\begin{aligned}
\mathcal{K}_{\text{RE}}^{\alpha,l}(T) &= \mathcal{K}_{\text{RE}}^{\alpha,l} f_l(m_{\text{RE}}(T)) \\
\mathcal{B}_{\text{RE}}^{X,l}(T) &= \mathcal{B}_{\text{RE}}^{X,l} f_l(m_{\text{RE}}(T))
\end{aligned} \tag{18}$$

and the RE subscript has been inserted as a reminder that the constants and order parameters are calculated either for TbFe<sub>2</sub> or DyFe<sub>2</sub>. The RE contribution for the Tb<sub>1-x</sub>Dy<sub>x</sub>Fe<sub>2</sub> alloy is obtained through the same linear mixing as at zero temperature, as in equation 7.

The temperature dependence of  $E_{\text{RE}}(\hat{\mathbf{n}}, \boldsymbol{\varepsilon}, T)$  is therefore fixed by the order parameter dependences  $m_{\text{Tb}}(T)$  and  $m_{\text{Dy}}(T)$ , which we determine through finite-temperature, LSIC DFT-DLM calculations on TbFe<sub>2</sub> and DyFe<sub>2</sub>. The calculations were performed according to the methodology described in detail in Ref. [48], and the reader is referred there for a more complete discussion of the underlying theory and technical details of the DFT-DLM scheme.

## 2. Thermally-averaged itinerant electron contribution

Performing the thermal average on  $E_{\text{itin}}$  gives, in analogy with equation 17,

$$\begin{aligned}
E_{\text{itin}}(\hat{\mathbf{n}}, \boldsymbol{\varepsilon}, T) &= \mathcal{B}_{\text{itin}}^{\gamma,2}(T) \sum_{i=1,2} \varepsilon^{\gamma i} S_i^{\gamma,2}(\hat{\mathbf{n}}) \\
&+ \mathcal{B}_{\text{itin}}^{\epsilon,2}(T) \sum_{i=1,2,3} \varepsilon^{\epsilon i} S_i^{\epsilon,2}(\hat{\mathbf{n}})
\end{aligned} \tag{19}$$

The finite temperature magnetoelastic constants are obtained from DFT-DLM calculations on GdFe<sub>2</sub>, which give directly the temperature dependence of  $\mathcal{B}_{\text{itin}}^{X,2}$ . As found previously for bcc Fe [33], the  $\mathcal{B}_{\text{itin}}^{X,2}$  constants do not follow an  $f_2(m_{\text{itin}})$  dependence on the order parameter. This observation reflects the itinerant origin of the magnetic anisotropy, compared to the single-ion description of the RE moments [49].

### 3. *The need for a phenomenological model*

It is reasonable to ask, given that LSIC DFT-DLM calculations can be used to obtain the itinerant electron magnetostriction and also the temperature dependence of the RE order parameters in  $\text{TbFe}_2$  and  $\text{DyFe}_2$ , why we should not perform the entire calculation in the DFT-DLM framework without any reference to crystal field theory. The technical difficulty is that the DFT-DLM calculations are performed within the atomic sphere approximation (ASA) [51], which means that nonspherical components of the potential at the RE site (i.e. the crystal field) are poorly described in the DFT-DLM calculation of the RE anisotropy. As a result, a separate treatment of the CF is required. In turn, it is important that the calculated energy contribution associated with the itinerant electron anisotropy is free of any contribution from the localized RE-4*f* electrons interacting with the CF, otherwise this contribution would be counted both in  $E_{\text{itin}}$  and  $E_{\text{RE}}$  in equation 1. Calculating the itinerant contribution for  $\text{GdFe}_2$ , which has no CF anisotropy, ensures that this is the case. Similarly, the assumptions of the CF model mean that the CF coefficients themselves should not depend on the asphericity of the RE-4*f* electrons. This requirement is satisfied by using the Y-analogue model, where the RE-4*f* electrons do not enter the calculation of the CF potential at all [25]. These same considerations led us to adopt a similar scheme in the calculation of finite temperature anisotropy of the  $\text{RCO}_5$  compounds [37].

### G. **Computational details**

Crystal field coefficients were calculated for  $\text{YFe}_2$  within the projector-augmented formulation of DFT as implemented in the GPAW code [52], using the local spin-density approximation (LSDA) for exchange and correlation [53]. A plane wave basis set with a 1200 eV energy cutoff and a  $20 \times 20 \times 20$   $k$ -point sampling was used, as in Ref. 25. A lattice constant of 7.341 Å was used throughout for the equilibrium (cubic) structure, which is the experimentally-measured value for  $\text{TbFe}_2$  at room temperature [54]; the value for  $\text{DyFe}_2$  is very similar (7.338 Å). The dependence of the order parameters on temperature were calculated within DFT-DLM [27] with the LSIC applied [48], using the ASA with Wigner-Seitz radii of 1.90 Å for the RE atoms, with angular momentum expansions truncated at  $l_{\text{max}} = 3$ . The same computational setup was used to calculate the temperature-dependent

	$\mathcal{K}^{\alpha,4}$	$\mathcal{K}^{\alpha,6}$	$\mathcal{B}^{\alpha,4}$	$\mathcal{B}^{\alpha,6}$	$\mathcal{B}^{\gamma,2}$	$\mathcal{B}^{\gamma,4}$	$\mathcal{B}^{\gamma,6}$	$\mathcal{B}^{\epsilon,2}$	$\mathcal{B}^{\epsilon,4}$	$\mathcal{B}^{\epsilon,6}$	$\mathcal{B}^{\epsilon,6'}$	$\mathcal{B}_{\text{itin}}^{\gamma,2}$	$\mathcal{B}_{\text{itin}}^{\epsilon,2}$
TbFe <sub>2</sub>	14.10	11.20	-22.87	-27.88	74.69	28.08	6.96	-844.24	258.17	7.22	-4.20	-7.25	33.24
DyFe <sub>2</sub>	-17.34	-47.52	28.14	116.89	77.12	-30.87	-29.43	-794.88	-307.96	-33.07	17.79	-7.25	33.24

TABLE I. Anisotropy and magnetoelastic constants in  $\text{MJm}^{-3}$  calculated for TbFe<sub>2</sub> and DyFe<sub>2</sub>.

magnetoelastic constants associated with the itinerant electrons for GdFe<sub>2</sub>, using the torque method as described in Refs. 33 and 49.

### III. RESULTS

#### A. Anisotropy and magnetoelastic constants

We previously reported Y-analogue calculations of the CF coefficients of TbFe<sub>2</sub> and DyFe<sub>2</sub> [25]. The values of  $\mathcal{K}^{\alpha,4}$  and  $\mathcal{K}^{\alpha,6}$  calculated from equation 11 are given in Table I. Importantly, due to the differences in  $\mathcal{A}_4$  and  $\mathcal{A}_6$  for Tb<sup>3+</sup> and Dy<sup>3+</sup>,  $\mathcal{K}^{\alpha,l}$  have opposite signs for TbFe<sub>2</sub> and DyFe<sub>2</sub> so favor different magnetization directions. From the linear mixing of equation 7, we note that a Dy content of  $x = 0.45$  would lead to a zero value of  $\mathcal{K}^{\alpha,4}$ .

Now considering the magnetoelastic constants associated with the RE, in Fig. 2 we plot the strain-induced change in the CF coefficients  $\Delta B_{lm}$  for TbFe<sub>2</sub>, for  $(l, m) = (2,0), (4,0)$  and  $(6,0)$ . We show  $\Delta B_{lm}$  for both tetragonal ( $\varepsilon_T$ ) and shear ( $\varepsilon_S$ ) strains. Following convention, we divide the CF coefficients by  $k_B$  so that the quantities have dimensions of temperature.

Although there is some numerical noise in  $\Delta B_{20}$  evident for small shear strains  $\varepsilon_S$ ,  $\Delta B_{lm}$  is linear in  $\varepsilon$  over the range of strains considered. Indeed, extending the calculations to larger shear strains confirms this linear relation out to at least  $\varepsilon_S = 0.01$  (inset of Fig. 2). Then, the most striking feature of Fig. 2 is the strong dependence of  $B_{20}$  on  $\varepsilon_S$ . At  $\varepsilon_S = 0.002$ ,  $\Delta B_{20}$  is 17 K, compared to 2 K for  $\varepsilon_T$  at -0.002. The corresponding difference between shear and tetragonal strains is much reduced at larger  $(l, m)$  values, with  $\Delta B_{40} = 4$  K and -1 K and  $\Delta B_{60} = 0$  K and 1 K respectively.

Converting these derivatives into magnetoelastic constants through relations like equation 12 gives the values shown in Table I. The large value of  $\frac{dB_{20}}{d\varepsilon_S}$  is reflected in the coefficient  $\mathcal{B}^{\epsilon,2}$ , which is an order of magnitude larger than  $\mathcal{B}^{\gamma,2}$ . Since  $\mathcal{B}^{\epsilon,2}$  is negative, this term will favor positive strains along [111]. Furthermore,  $\mathcal{B}^{\epsilon,2}$  is the same sign for both TbFe<sub>2</sub> and

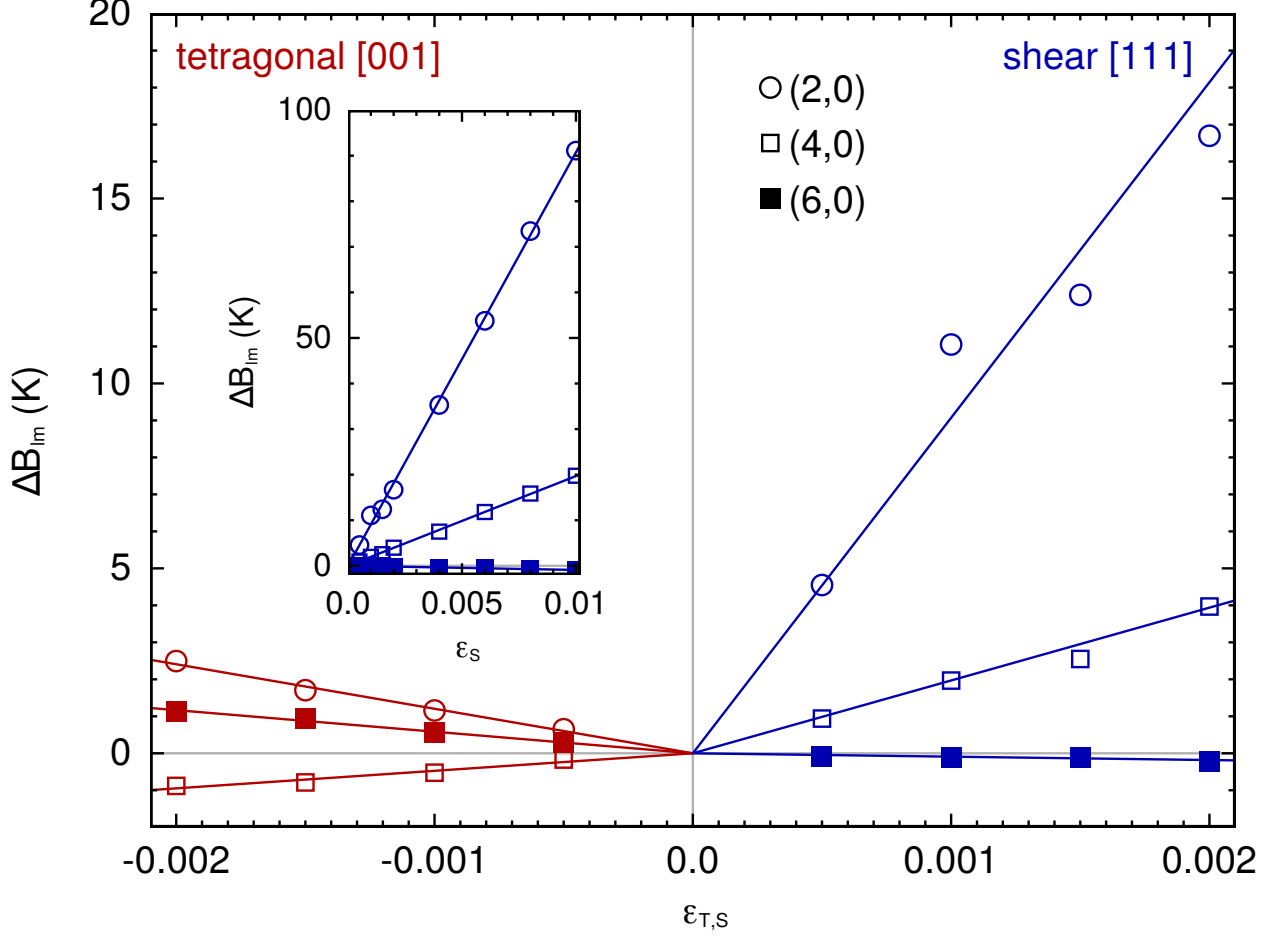


FIG. 2. Change in crystal field coefficients  $\Delta B_{lm}$  for  $\text{TbFe}_2$  for different  $(l, m)$  with a shear strain  $\epsilon_S$  (blue) or a tetragonal strain  $\epsilon_T$  (red) applied. The inset shows  $\Delta B_{lm}$  for a larger variation in  $\epsilon_S$ . The straight lines are fits to the calculations.

$\text{DyFe}_2$ , since  $\mathcal{A}_2$  is identical for  $\text{Tb}^{3+}$  and  $\text{Dy}^{3+}$  [38, 39]. Therefore, unlike  $\mathcal{K}^{\alpha,4}$ , there is no cancellation of  $\mathcal{B}^{\epsilon,2}$  in the alloy. It is this aspect which allows  $\text{Tb}_{1-x}\text{Dy}_x\text{Fe}_2$  to have simultaneously a large magnetostriction and small anisotropy.

Now considering the itinerant electrons, our DFT-DLM calculations on  $\text{GdFe}_2$  find the contribution to the MCA to be negligible (of order  $1 \text{ Jm}^{-3}$ ). The magnetoelastic constants are more significant, and their zero temperature values are given in Table I (we stress again that their temperature dependence is more complicated than  $f_l(m)$ ) [33]. The magnetoelastic contribution is well described by constants with  $l = 2$  only.  $\mathcal{B}_{\text{Fe}}^{\gamma,2}$  and  $\mathcal{B}_{\text{Fe}}^{\epsilon,2}$  are calculated to have the same sign as observed experimentally for bcc Fe [55], but their magnitudes are enhanced ( $-7.1$  and  $33 \text{ MJm}^{-3}$ ). However, the itinerant electrons still contribute much less



than the RE at all of the temperatures considered here.

### B. Easy directions and magnetostrictions at zero temperature

Using the constants reported in Table I we can construct the phenomenological energy for an arbitrary strain, magnetization and composition. Considering the zero temperature case first (equation 1), minimizing  $E(\hat{\boldsymbol{\epsilon}}, \boldsymbol{\epsilon})$  with respect to magnetization direction and strain for the end compounds TbFe<sub>2</sub> and DyFe<sub>2</sub> finds easy directions of [111] and [100] respectively. The calculated fractional changes in length along [111] and [100] for TbFe<sub>2</sub> and DyFe<sub>2</sub> are  $\lambda_{111}^{\text{TbFe}_2} = 5200$  ppm and  $\lambda_{100}^{\text{DyFe}_2} = -780$  ppm at 0 K. Comparing to experimentally-measured values of 4400 and -70 ppm [3] shows correct qualitative behaviour and numerical agreement within  $\sim 1000$  ppm, or 0.1% strain; in relative terms, the agreement for  $\lambda_{100}^{\text{DyFe}_2}$  is less good than for TbFe<sub>2</sub>.

Now considering the alloy through equation 7 we find a [111] easy direction for all values of  $x$  below  $x_c = 0.56$ , above which the easy direction switches abruptly to [100]. This is some way off the experimental optimal concentration of  $x = 0.73$ , but we have not yet included temperature effects. It is also interesting to recompute the magnetization direction ignoring the magnetoelastic contribution to the energy. Then,  $x_c$  is found to be 0.45, the same value which cancelled  $\mathcal{K}^{\alpha,4}$ .

### C. Spin orientation diagram

We now consider finite temperature, and minimize  $E(\hat{\boldsymbol{n}}, \boldsymbol{\epsilon}, T)$  (equation 13) for a grid of  $(x, T)$  values. The resulting spin orientation diagram is shown in Fig. 3. As at zero temperature, the easy directions are found either to be [111] or [100] (blue or red regions), and increased Dy content favours [100] magnetization. However, at higher temperatures more Dy is required to maintain the [100] magnetization, i.e.  $x_c$  increases with temperature.

The reason for the increase in  $x_c$  is due to the behavior of the RE order parameters with temperature. Our DFT-DLM calculations find that the Dy order parameter  $m_{\text{Dy}}$  decreases more quickly with  $T$  than  $m_{\text{Tb}}$ , something which can also be inferred from experimental magnetization measurements [26]. This behavior can be understood as the lower spin moment of Dy weakening the exchange interaction [14]. Since  $\mathcal{K}^{\alpha,4}$  is highly sensitive to  $m$

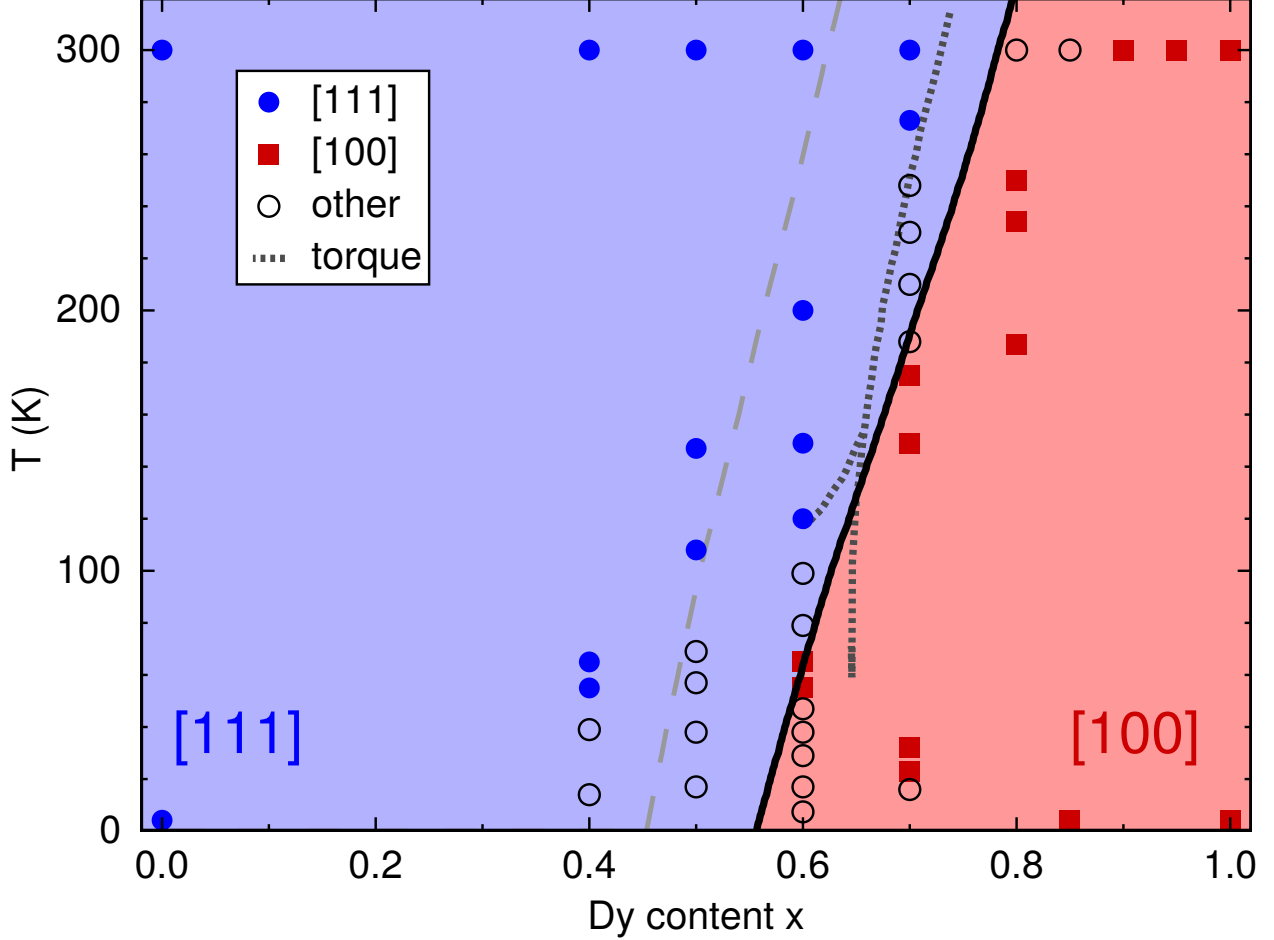


FIG. 3. The easy direction of magnetization of  $\text{Tb}_{1-x}\text{Dy}_x\text{Fe}_2$ , calculated by minimizing  $E(\hat{n}, \varepsilon, x, T)$  (red and blue shaded regions). The symbols are experimental measurements of the easy direction using Mössbauer spectroscopy [20, 56]. The dotted lines mark the boundaries between different magnetization directions extracted from torque magnetometry [57], where above 150 K the boundary is between [111] and [100], and below encloses a region of intermediate magnetization direction. The dashed line is the [111]/[100] boundary obtained by minimizing  $E_{\text{MCA}}$  only.

( $\sim m^{10}$ , thanks to  $f_4(m)$ ), more Dy is required at higher temperatures to maintain the [100] magnetization.

Our calculated value of  $x_c$  at 300 K is  $x_c = 0.78$ . At this concentration we calculate magnetostrictions of  $\lambda_{111}=2700$  and  $\lambda_{100}=-430$  ppm. As at zero temperature with the end compounds, the calculated values are within  $\sim 1000$  ppm of the experimental ones, as measured at 300 K for Terfenol-D [1].

Like for the zero temperature case, we also calculated the spin orientation ignoring the magnetoelastic terms in the energy. The boundary between the [111] and [100] easy directions in this case is shown as the grey dashed line in Fig. 3. The shifted line can be understood from Fig. 2 and surrounding discussion:  $\mathcal{B}^{\epsilon,2}$  is large, so while the magnetization points along [111] the material can save energy by distorting. Switching off the magnetoelastic contribution reduces the region where [111] magnetization is favorable, so less Dy is required to make the transition to [100].

Figure 3 also shows experimental measurements of the easy magnetization direction obtained from Mössbauer spectroscopy [20, 56], and torque magnetometry measurements of the  $(x, T)$  boundaries between different magnetization orientations [57]. Our calculations agree with all of the measurements of the [111] and [100] easy directions across different temperatures and compositions (no red symbols appear on blue, and vice versa). However, the open circles in Fig. 3 are measurements where the magnetization points along  $[uv0]$  or  $[uvw]$  rather than [111] or [100] [56]. Our calculations do not capture these intermediate directions, as we shall discuss in the concluding section.

#### IV. OUTLOOK

We first return to the original question of our work concerning Terfenol-D's optimum dysprosium content,  $x=0.73$ . Our calculations actually find that the entire composition range of  $\text{Tb}_{1-x}\text{Dy}_x\text{Fe}_2$  is remarkable for having highly anisotropic magnetostrictions. For instance, we find that the end compounds have  $\lambda_{111}^{\text{DyFe}_2} = 5640$  and  $\lambda_{100}^{\text{TbFe}_2} = -970$  ppm at 0 K (compare to  $\lambda_{111}^{\text{TbFe}_2} = 5200$  ppm and  $\lambda_{100}^{\text{DyFe}_2} = -780$  ppm reported above). However, what is critical for applications is the ability to rotate the magnetization direction at small fields [26], i.e. a small MCA, which is achieved at  $x_c$  where the easy direction switches. Our calculated value of  $x_c=0.78$  at 300 K rationalizes the experimentally-determined critical concentration from first principles. We stress that we get a very different value if we ignore temperature ( $x_c=0.56$ ) or magnetostriction ( $x_c=0.62$ ).

Interestingly our calculations have not captured a more subtle feature of the spin orientation diagram, which is the presence of  $[uv0]$  or  $[uvw]$  easy magnetization directions (open circles in Fig. 3) [56]. The reason for this discrepancy is in our first-order treatment of the CF, which generates terms up to  $l = 6$  in equation 1. In order to describe  $[uv0]$  or

[ $uvw$ ] easy directions, the energy must contain terms with larger  $l$  [24, 58]. To proceed, we should go beyond the first-order perturbative treatment of the CF (equation 9) and instead construct the full RE-4*f* Hamiltonian including the CF potential and the exchange field, and diagonalize it within the  $M_J$  manifold [37]. A complete treatment would map out the strain dependence of all terms within the Hamiltonian. This approach could potentially find intermediate easy directions and also allow us to calculate the dependence of Tb<sub>1-x</sub>Dy<sub>x</sub>Fe<sub>2</sub> magnetostriction on the external field. Our test calculations using a finite exchange field have indeed found intermediate easy directions for small  $T$  and  $x \sim 0.5$ , indicating that this is a promising direction for future work.

A further refinement is to account for internal distortions within the unit cell. Indeed, the classic work of Cullen and Clark [59] argued that the internal distortion could provide the key to explaining the huge anisotropy in magnetostriction between the [111] and [100] directions. However, as was shown by the zero temperature calculations of Ref. [16] and reiterated here,  $\lambda_{111}$  is found to be much larger than  $\lambda_{100}$  even when no internal distortions are taken into account. Our test calculations of the CF coefficients along different frozen phonon modes have found the variation to be small compared to applying a global strain. However, the (zero temperature) calculations of Ref. [16] did find a reduction in  $\lambda_{111}^{\text{TbFe}_2}$  of 1300 ppm when they included an internal distortion, which would bring our value closer to experiment. Therefore, it is important to investigate the inclusion of all possible distortions and couplings at a consistent level.

An additional question concerns the use of the single-ion approximation (e.g. equation 7). This approximation is generally understood to work very well for rare-earth/transition-metal magnets like REFe<sub>2</sub> [32]. However, it is reasonable to ask to what extent the crystal field parameters and the exchange field at the RE site might be influenced by fluctuations in its surroundings, including those caused by other RE atoms. Employing our methodology on supercells incorporating such fluctuations will allow this question to be addressed.

Going beyond Terfenol-D, having validated the methodology we can now evaluate other materials' magnetostrictive properties, ideally with reduced RE content. The ability to calculate phase boundaries is of particular interest to the design of multiferroic architectures, where working at such boundaries will maximise the response [9]. For instance, we could easily simulate epitaxial strain by adding additional strain to our calculations or, more ambitiously, model the explicit effects of the interface on the CF. Intriguingly, the calculations

	$c_{11}$	$c_{12}$	$c_{44}$
Tb <sub>0.3</sub> Dy <sub>0.7</sub> Fe <sub>2</sub> , exp. [26]	141	65	49
DyFe <sub>2</sub> , exp. [26]	146	68	47
TbFe <sub>2</sub> , calc. [30]	197	112	84
YFe <sub>2</sub> , calc. [31]	206	132	50

TABLE II. Elastic constants, in GPa either measured experimentally (exp.) or calculated (calc.) for different compounds.

also show that there exists a basic property of the Laves phase structure, perhaps the orientation of RE-RE bonds, which makes the CF highly sensitive to shear strain. Elucidating this mechanism could help design more magnetostrictive materials.

## ACKNOWLEDGMENTS

The present work forms part of the PRETAMAG project, funded by the UK Engineering and Physical Sciences Research Council, Grant No. EP/M028941/1.

## Appendix: Elastic constants

In our calculations of the elastic energy (Sec. II A 1) we used the values of the elastic constants  $c_{11}$ ,  $c_{12}$  and  $c_{44}$  measured experimentally [26] for Tb<sub>0.3</sub>Dy<sub>0.7</sub>Fe<sub>2</sub> for all compositions and temperatures. Here we illustrate the effect on the spin orientation diagram of using different values for these constants. Table II lists elastic constants either measured experimentally for Tb<sub>0.3</sub>Dy<sub>0.7</sub>Fe<sub>2</sub> and DyFe<sub>2</sub> [26], or calculated within DFT for TbFe<sub>2</sub> and YFe<sub>2</sub> [30, 31]. For the DFT calculations a generalized-gradient approximation (GGA) was used for the exchange correlation. We include YFe<sub>2</sub> due to it having the same valence electronic structure.

We recalculated the spin orientation diagram for each set of constants and show the result in Fig. 4. The qualitative structure of the diagram for each set of constants is identical, consisting of a single boundary between [111] and [100] easy directions. Quantitatively, the three sets of elastic constants corresponding to Tb<sub>0.3</sub>Dy<sub>0.7</sub>Fe<sub>2</sub> and DyFe<sub>2</sub> (experimental) and YFe<sub>2</sub> [30, 31] (calculated) give effectively identical boundaries. Using the elastic constants

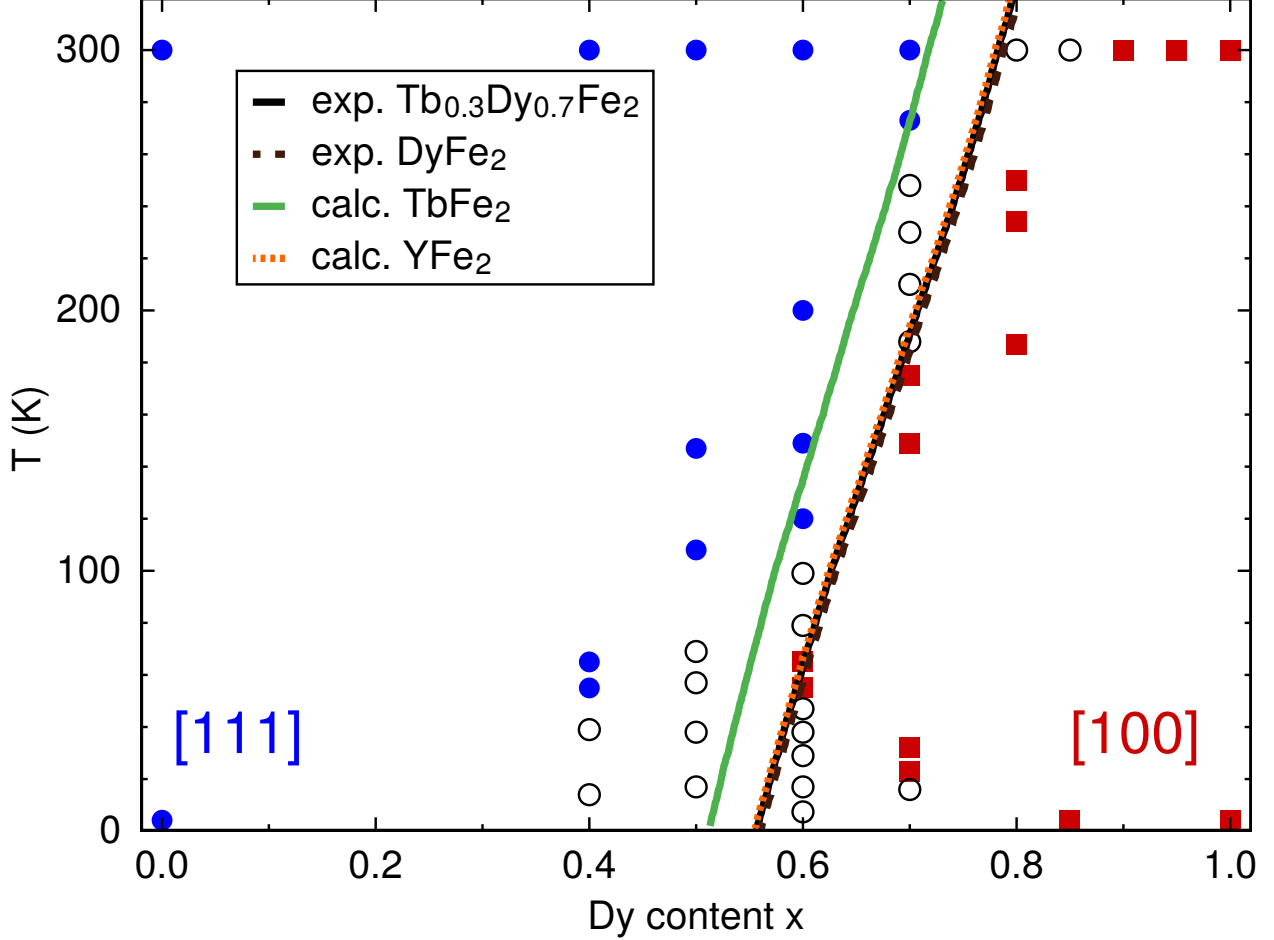


FIG. 4. The spin orientation diagram of  $\text{Tb}_{1-x}\text{Dy}_x\text{Fe}_2$  calculated with different sets of elastic constants. The same experimental data is shown as in Fig. 3. The diagonal lines represent the boundaries between [111] and [100] directions of magnetization for the different sets of elastic constants listed in Table II.

calculated for  $\text{TbFe}_2$  shifts the critical concentration  $x_c$  down by approximately 0.05, such that  $x_c = 0.51$  at 0 K and  $x_c = 0.72$  at 300 K. Examining Table II would indicate that the critical concentration is most sensitive to  $c_{44}$ , which is reasonable given crucial role played by the large [111] magnetostriction.

We note that using the elastic constants calculated for  $\text{TbFe}_2$  brings the room temperature critical concentration to within 0.01 of the experimental Terfenol-D value. However, since it is not clear that a GGA treatment is sufficiently accurate to describe the Tb-4*f* electrons [30, 48], in this work we prefer to use experimental values for the elastic constants. Furthermore, the effectively identical results for  $\text{Tb}_{0.3}\text{Dy}_{0.7}\text{Fe}_2$  and  $\text{DyFe}_2$ , and the weak sensitivity to  $c_{ij}$

in general, justifies the use of a single set of elastic constants for the entire spin orientation diagram.

- 
- [1] R. Abbundi and A. Clark, Anomalous thermal expansion and magnetostriction of single crystal  $\text{Tb}_{.27}\text{Dy}_{.73}\text{Fe}_2$ , *IEEE Trans. Magn.* **13**, 1519 (1977).
  - [2] A. E. Clark, High-field magnetization and coercivity of amorphous rare-earth- $\text{Fe}_2$  alloys, *Appl. Phys. Lett.* **23**, 642 (1973).
  - [3] A. Clark, R. Abbundi, H. Savage, and O. McMasters, Magnetostriction of rare earth- $\text{Fe}_2$  Laves phase compounds, *Physica B+C* **86-88**, 73 (1977).
  - [4] E. du Trémolet de Lacheisserie, *Magnetostriction: Theory and Applications of Magnetoelasticity* (CRC Press, 1993).
  - [5] M. E. Staley and A. B. Flatau, Characterization of energy harvesting potential of Terfenol-D and Gallenol, in *Smart Structures and Materials 2005: Smart Structures and Integrated Systems*, Vol. 5764, edited by A. B. Flatau, International Society for Optics and Photonics (SPIE, 2005) pp. 630 – 640.
  - [6] Z. Deng and M. J. Dapino, Review of magnetostrictive vibration energy harvesters, *Smart Mater. Struct.* **26**, 103001 (2017).
  - [7] J. Rudd and O. Myers, Experimental fabrication and nondestructive testing of carbon fiber beams for delaminations using embedded Terfenol-D particles, *J. Intel. Mat. Syst. Str.* **29**, 600 (2018).
  - [8] Q. Wang, X. Li, C.-Y. Liang, A. Barra, J. Domann, C. Lynch, A. Sepulveda, and G. Carman, Strain-mediated  $180^\circ$  switching in CoFeB and Terfenol-D nanodots with perpendicular magnetic anisotropy, *Appl. Phys. Lett.* **110**, 102903 (2017).
  - [9] D. Li, X.-M. Zhao, H.-X. Zhao, X.-W. Dong, L.-S. Long, and L.-S. Zheng, Construction of Magnetoelectric Composites with a Large Room-Temperature Magnetoelectric Response through Molecular-Ionic Ferroelectrics, *Advanced Materials* **30**, 1803716 (2018).
  - [10] J. Atulasimha and A. B. Flatau, A review of magnetostrictive iron–gallium alloys, *Smart Mater. and Struct.* **20**, 043001 (2011).
  - [11] J. D. S. Vincent, M. Rodrigues, Z. Leong, and N. A. Morley, Design and Development of Magnetostrictive Actuators and Sensors for Structural Health Monitoring, *Sensors* **20**, 711

- (2020).
- [12] A. E. Clark, K. B. Hathaway, M. Wun-Fogle, J. B. Restorff, T. A. Lograsso, V. M. Keppens, G. Petculescu, and R. A. Taylor, Extraordinary magnetoelasticity and lattice softening in bcc Fe-Ga alloys, *J. Appl. Phys.* **93**, 8621 (2003).
  - [13] A. E. Clark, J. B. Restorff, M. Wun-Fogle, D. Wu, and T. A. Lograsso, Temperature dependence of the magnetostriction and magnetoelastic coupling in  $\text{Fe}_{100-x}\text{Al}_x$  ( $x=14.1,16.6,21.5,26.3$ ) and  $\text{Fe}_{50}\text{Co}_{50}$ , *J. Appl. Phys.* **103**, 07B310 (2008).
  - [14] M. S. S. Brooks, L. Nordström, and B. Johansson, 3d-5d band magnetism in rare earth-transition metal intermetallics: total and partial magnetic moments of the  $\text{RFe}_2$  ( $\text{R}=\text{Gd-Yb}$ ) Laves phase compounds, *J. Phys.: Condens. Matter* **3**, 2357 (1991).
  - [15] M. Richter, Band structure theory of magnetism in 3d-4f compounds, *J. Phys. D: Appl. Phys.* **31**, 1017 (1998).
  - [16] S. Buck and M. Fähnle, Magnetostriction in  $\text{TbFe}_2$ : weak influence of the internal structural distortion, *J. Magn. Magn. Mater.* **204**, L1 (1999).
  - [17] V. I. Gavrilenko and R. Q. Wu, Magnetostriction and magnetism of rare earth intermetallic compounds: First principle study, *J. Appl. Phys.* **89**, 7320 (2001).
  - [18] M. Fähnle and F. Welsch, From the electronic structure to the macroscopic magnetic behaviour of rare-earth intermetallics: a combination of ab initio electron theory with statistical mechanics and elasticity theory, *Physica B: Condens. Matt.* **321**, 198 (2002).
  - [19] H. Wang, Y. N. Zhang, R. Q. Wu, L. Z. Sun, D. S. Xu, and Z. D. Zhang, Understanding strong magnetostriction in  $\text{Fe}_{100-x}\text{Ga}_x$  alloys, *Sci. Rep.* **3**, 3521 (2013).
  - [20] U. Atzmony, M. P. Dariel, E. R. Bauminger, D. Lebenbaum, I. Nowik, and S. Ofer, Spin-Orientation Diagrams and Magnetic Anisotropy of Rare-Earth-Iron Ternary Cubic Laves Compounds, *Phys. Rev. B* **7**, 4220 (1973).
  - [21] N. C. Koon and C. M. Williams, Origins of magnetic anisotropy in cubic  $\text{RFe}_2$  Laves phase compounds, *J. Appl. Phys.* **49**, 1948 (1978).
  - [22] M. D. Kuz'min, Magnetostriction of  $\text{DyFe}_2$  and  $\text{HoFe}_2$ : Validity of the single-ion model, *J. Appl. Phys.* **89**, 5592 (2001).
  - [23] G. J. Bowden, P. A. J. de Groot, J. D. O'Neil, B. D. Rainford, and A. A. Zhukov, On the anomalous temperature-dependent magnetostriction in intermetallic  $\text{DyFe}_2$ , *J. Phys. Condens. Matter* **16**, 2437 (2004).



- [24] K. N. Martin, P. A. J. de Groot, B. D. Rainford, K. Wang, G. J. Bowden, J. P. Zimmermann, and H. Fangohr, Magnetic anisotropy in the cubic Laves REFe<sub>2</sub> intermetallic compounds, *J. Phys.: Condens. Matter* **18**, 459 (2006).
- [25] C. E. Patrick and J. B. Staunton, Crystal field coefficients for yttrium analogues of rare-earth/transition-metal magnets using density-functional theory in the projector-augmented wave formalism, *J. Phys.: Condens. Matter* **31**, 305901 (2019).
- [26] A. Clark, Magnetostrictive Rare Earth-Fe<sub>2</sub> Compounds, in *Handbook of Ferromagnetic Materials*, Vol. 1 (Elsevier, 1980) p. 531.
- [27] B. L. Györfy, A. J. Pindor, J. Staunton, G. M. Stocks, and H. Winter, A first-principles theory of ferromagnetic phase transitions in metals, *J. Phys. F: Met. Phys.* **15**, 1337 (1985).
- [28] We note that in a ferrimagnet like REFe<sub>2</sub>, the itinerant electron magnetic sublattice may be oriented *antiparallel* to  $\hat{e}$ ; however this detail does not affect our discussion, since  $E_{\text{itin}}(\hat{e}, \varepsilon) = E_{\text{itin}}(-\hat{e}, \varepsilon)$ .
- [29] C. Kittel, Physical theory of ferromagnetic domains, *Rev. Mod. Phys.* **21**, 541 (1949).
- [30] A. Bentouaf, R. Mebsout, H. Rached, S. Amari, A. Reshak, and B. Aïssa, Theoretical investigation of the structural, electronic, magnetic and elastic properties of binary cubic C15-Laves phases TbX<sub>2</sub> (X=Co and Fe), *J. Alloys Compd.* **689**, 885 (2016).
- [31] N. Moulay, H. Rached, M. Rabah, S. Benalia, D. Rached, A. H. Reshak, N. Benkhattou, and P. Ruterana, First-principles calculations of the elastic, and electronic properties of YFe<sub>2</sub>, NiFe<sub>2</sub> and YNiFe<sub>4</sub> intermetallic compounds, *Comp. Mater. Sci.* **73**, 56 (2013).
- [32] M. D. Kuz'min and A. M. Tishin, Theory of Crystal-Field Effects in *3d-4f* Intermetallic Compounds, in *Handbook of Magnetic Materials*, Vol. 17 (Elsevier, 2008) p. 149.
- [33] G. A. Marchant, C. E. Patrick, and J. B. Staunton, *Ab initio* calculations of temperature-dependent magnetostriction of Fe and A<sub>2</sub>Fe<sub>1-x</sub>Ga<sub>x</sub> within the disordered local moment picture, *Phys. Rev. B* **99**, 054415 (2019).
- [34] H. Callen and E. Callen, The present status of the temperature dependence of magnetocrystalline anisotropy, and the  $l(l+1)/2$  power law, *J. Phys. Chem. Solids* **27**, 1271 (1966).
- [35] M. Loewenhaupt, P. Tils, K. Buschow, and R. Eccleston, Exchange interactions in GdFe compounds studied by inelastic neutron scattering, *J. Magn. Magn. Mater.* **152**, 10 (1996).
- [36] J. S. Griffith, *The Theory of Transition-Metal Ions* (Cambridge University Press, 1961).
- [37] C. E. Patrick and J. B. Staunton, Temperature-dependent magnetocrystalline anisotropy of

- rare earth/transition metal permanent magnets from first principles: The light  $R\text{Co}_5$  ( $R = \text{Y, La-Gd}$ ) intermetallics, *Phys. Rev. Materials* **3**, 101401 (2019).
- [38] J. Sievers, Asphericity of  $4f$ -shells in their Hund's rule ground states, *Z. Phys. B* **45**, 289 (1982).
- [39] K. W. H. Stevens, Matrix Elements and Operator Equivalents Connected with the Magnetic Properties of Rare Earth Ions, *Proc. Phys. Soc. A* **65**, 209 (1952).
- [40] A. R. Edmonds, Angular momentum in quantum mechanics (Princeton University Press, Princeton, New Jersey, 1960) Chap. 4, p. 59.
- [41] C. J. Bradley and A. P. Cracknell, *The Mathematical Theory of Symmetry in Solids* (Oxford University Press, 1972) Chap. 3, p. 82.
- [42] S. Kumar, C. E. Patrick, R. S. Edwards, G. Balakrishnan, M. R. Lees, and J. B. Staunton, Torque magnetometry study of the spin reorientation transition and temperature-dependent magnetocrystalline anisotropy in  $\text{NdCo}_5$ , *J. Phys.: Condens. Matter* **32**, 255802 (2020).
- [43] S. Kumar, C. E. Patrick, R. S. Edwards, G. Balakrishnan, M. R. Lees, and J. B. Staunton, Tunability of the spin reorientation transitions with pressure in  $\text{NdCo}_5$ , *Appl. Phys. Lett.* **116**, 102408 (2020).
- [44] M. Lüders, A. Ernst, M. Däne, Z. Szotek, A. Svane, D. Ködderitzsch, W. Hergert, B. L. Györfy, and W. M. Temmerman, Self-interaction correction in multiple scattering theory, *Phys. Rev. B* **71**, 205109 (2005).
- [45] M. Däne, M. Lüders, A. Ernst, D. Ködderitzsch, W. M. Temmerman, Z. Szotek, and W. Hergert, Self-interaction correction in multiple scattering theory: application to transition metal oxides, *J. Phys. Condens. Matter* **21**, 045604 (2009).
- [46] These functions were reported previously in Ref. [25], Fig. 1 and are available on request.
- [47] C. E. Patrick, S. Kumar, G. Balakrishnan, R. S. Edwards, M. R. Lees, L. Petit, and J. B. Staunton, Calculating the Magnetic Anisotropy of Rare-Earth/Transition-Metal Ferrimagnets, *Phys. Rev. Lett.* **120**, 097202 (2018).
- [48] C. E. Patrick and J. B. Staunton, Rare-earth/transition-metal magnets at finite temperature: Self-interaction-corrected relativistic density functional theory in the disordered local moment picture, *Phys. Rev. B* **97**, 224415 (2018).
- [49] J. B. Staunton, L. Szunyogh, A. Buruzs, B. L. Györfy, S. Ostanin, and L. Udvardi, Temperature dependence of magnetic anisotropy: An *ab initio* approach, *Phys. Rev. B* **74**, 144411

- (2006).
- [50] C. E. Patrick, S. Kumar, G. Balakrishnan, R. S. Edwards, M. R. Lees, E. Mendive-Tapia, L. Petit, and J. B. Staunton, Rare-earth/transition-metal magnetic interactions in pristine and (Ni,Fe)-doped  $\text{YCo}_5$  and  $\text{GdCo}_5$ , *Phys. Rev. Materials* **1**, 024411 (2017).
  - [51] B. L. Györfy and G. M. Stocks, First principles band theory for random metallic alloys, in *Electrons in Disordered Metals and at Metallic Surfaces*, Nato Science Series B, edited by P. Phariseau and B. Györfy (Springer US, 1979) Chap. 4, pp. 89–192.
  - [52] J. Enkovaara, C. Rostgaard, J. J. Mortensen, J. Chen, M. Dułak, L. Ferrighi, J. Gavnholt, C. Glinsvad, V. Haikola, H. A. Hansen, *et al.*, Electronic structure calculations with GPAW: a real-space implementation of the projector augmented-wave method, *J. Phys. Condens. Matter* **22**, 253202 (2010).
  - [53] S. H. Vosko, L. Wilk, and M. Nusair, Accurate spin-dependent electron liquid correlation energies for local spin density calculations: a critical analysis, *Can. J. Phys.* **58**, 1200 (1980).
  - [54] A. V. Andreev, Thermal expansion anomalies and spontaneous magnetostriction in rare-earth intermetallics with cobalt and iron, in *Handbook of Magnetic Materials*, Vol. 8, edited by K. H. J. Buschow (Elsevier North-Holland, New York, 1995) Chap. 2, p. 59.
  - [55] G. Wedler, J. Walz, A. Greuer, and R. Koch, The magnetoelastic coupling constant  $B_2$  of epitaxial Fe(001) films, *Surf. Sci.* **454-456**, 896 (2000).
  - [56] U. Atzmony, M. P. Dariel, and G. Dublon, Spin-orientation diagram of the pseudobinary  $\text{Tb}_{1-x}\text{Dy}_x\text{Fe}_2$  Laves compounds, *Phys. Rev. B* **15**, 3565 (1977).
  - [57] C. Williams, N. Koon, and B. Das, Torque measurements on single crystal  $\text{Dy}_x\text{Tb}_{1-x}\text{Fe}_2$  compounds, *J. Magn. Magn. Mater.* **15-18**, 553 (1980).
  - [58] U. Atzmony and M. P. Dariel, Nonmajor cubic symmetry axes of easy magnetization in rare-earth-iron Laves compounds, *Phys. Rev. B* **13**, 4006 (1976).
  - [59] J. R. Cullen and A. E. Clark, Magnetostriction and structural distortion in rare-earth intermetallics, *Phys. Rev. B* **15**, 4510 (1977).